dot, so there should always be a step at the start of the pulse. The fraction of traces in which this step is nevertheless missed, that is, ΔI_{QPC} stays below the threshold (blue line in Fig. 3d), gives β_2. We plot $1-\beta_2$ in Fig. 4b (open dots). The resulting total fidelity for spin-↓ is given by $1-\beta \approx (1-\beta_1)(1-\beta_2)+(\alpha\beta_1)$. The last term accounts for the case when a spin-↓ electron is flipped to spin-↑, but there is nevertheless a step in ΔI_{QPC} due to the dark-count mechanism. In Fig. 4b we also plot the extracted value of $1-\beta$ as a function of the threshold.

We now choose the optimal value of the threshold as the one for which the visibility $1-\alpha-\beta$ is maximal (red line in Fig. 4b). For this setting, $\alpha \approx 0.07$, $\beta_1 \approx 0.17$ and $\beta_2 \approx 0.15$, so the measurement fidelity for the spin-↑ and the spin-↓ state is ~0.93 and ~0.72, respectively. The measurement visibility in a single-shot measurement is thus at present 65%.

Significant improvements in the spin measurement visibility can be made by lowering the electron temperature (smaller α), and especially by making the charge measurement faster (smaller β). Already, the demonstration of single-shot spin read-out and the observation of T_1 of the order of 1 ms are encouraging results for the use of electron spins as quantum bits. Present experiments focus on measuring the phase coherence time, T_2 (by definition $\leq 2T_1$), by performing pulsed electron spin resonance experiments. □

Received 6 April; accepted 25 May 2004; doi:10.1038/nature02693.

1. Sakurai, J. J. *Modern Quantum Mechanics* (Addison-Wesley, Reading, Massachusetts, 1994).
2. Wehrli, F. W. The origins and nature of nuclear magnetic resonance imaging. *Phys. Today* **6,** 34–42 (1992).
3. Wolf, S. A. *et al.* Spintronics: a spin-based electronics vision for the future. *Science* **294,** 1488–1495 (2001).
4. Blatt, R. & Zoller, P. Quantum jumps. *Eur. J. Phys.* **9,** 250–279 (1988).
5. Rugar, D., Budakian, R., Mamin, H. J. & Chui, B. W. Single spin detection by magnetic resonance force microscopy. *Nature* **430,** 329–332 (2004).
6. Loss, D. & DiVincenzo, D. P. Quantum computation with quantum dots. *Phys. Rev. A* **57,** 120–126 (1998).
7. Kane, B. E. A silicon-based nuclear spin quantum computer. *Nature* **393,** 133–137 (1998).
8. Vandersypen, L. M. K., *et al.* in *Quantum Computing and Quantum Bits in Mesoscopic Systems* (eds Legget, A. J., Ruggiero, B. & Silvestrini, P.) 201–209 (Kluwer Academic/Plenum, New York, 2003); ⟨http://xxx.lanl.gov/abs/quant-ph/0207059⟩ (2002).
9. Xiao, M., Martin, I. & Jiang, H. W. Probing the spin state of a single electron trap by random telegraph signal. *Phys. Rev. Lett.* **91,** 078301 (2003).
10. Friesen, M., Tahan, C., Joynt, R. & Eriksson, M. A. Spin readout and initialization in a semiconductor quantum dot. *Phys. Rev. Lett.* **92,** 037901 (2004).
11. Engel, H. *et al.* Measurement efficiency and n-shot read out of spin qubits. *Phys. Rev. Lett.* (in the press); preprint at ⟨http://xxx.lanl.gov/abs/cond-mat/0309023⟩ (2003).
12. Ionicioiu, R. & Popescu, A. E. Single spin measurement using spin-orbital entanglement. Preprint at ⟨http://xxx.lanl.gov/abs/quant-ph/0310047⟩ (2003).
13. Greentree, A. D., Hamilton, A. R., Hollenberg, L. C. L. & Clark, R. G. Electrical readout of a spin qubit without double occupancy. Preprint at ⟨http://xxx.lanl.gov/abs/cond-mat/0403449⟩ (2004).
14. Kouwenhoven, L. P., Austing, D. G. & Tarucha, S. Few-electron quantum dots. *Rep. Prog. Phys.* **64,** 701–736 (2001).
15. Weis, J., Haug, R. J., von Klitzing, K. & Ploog, K. Lateral transport through a single quantum dot with a magnetic field parallel to the current. *Surf. Sci.* **305,** 664–668 (1994).
16. Kouwenhoven, L. P. *et al.* Excitation spectra of circular, few-electron quantum dots. *Science* **278,** 1788–1792 (1997).
17. Ciorga, M. *et al.* Readout of a single electron spin based quantum bit by current detection. *Physica E* **11,** 35–40 (2001).
18. Fujisawa, T., Austing, D. G., Tokura, Y., Hirayama, Y. & Tarucha, S. Allowed and forbidden transitions in artificial hydrogen and helium atoms. *Nature* **419,** 278–281 (2002).
19. Hanson, R. *et al.* Zeeman energy and spin relaxation in a one-electron quantum dot. *Phys. Rev. Lett.* **91,** 196802 (2003).
20. Folk, J. A., Potok, R. M., Marcus, C. M. & Umansky, V. A gate-controlled bidirectional spin filter using quantum coherence. *Science* **299,** 679–682 (2003).
21. Lu, W., Ji, Z., Pfeiffer, L., West, K. W. & Rimberg, A. J. Real-time detection of electron tunnelling in a quantum dot. *Nature* **423,** 422–425 (2003).
22. Fujisawa, T., Hayashi, T., Hirayama, Y., Cheong, H. D. & Jeong, Y. H. Electron counting of single-electron tunnelling current. *Appl. Phys. Lett.* **84,** 2343–2345 (2004).
23. Elzerman, J. M. *et al.* Few-electron quantum dot circuit with integrated charge read out. *Phys. Rev. B* **67,** 161308 (2003).
24. Elzerman, J. M., Hanson, R., Willems van Beveren, L. H., Vandersypen, L. M. K. & Kouwenhoven, L. P. Excited-state spectroscopy on a nearly-closed quantum dot via charge detection. *Appl. Phys. Lett.* **84,** 4617–4619 (2004).
25. Field, M. *et al.* Measurements of Coulomb blockade with a noninvasive voltage probe. *Phys. Rev. Lett.* **70,** 1311–1314 (1993).
26. Hanson, R. *et al.* Semiconductor few-electron quantum dot operated as a bipolar spin filter. Preprint at ⟨http://xxx.lanl.gov/abs/cond-mat/0311414⟩ (2003).
27. Khaetskii, A. V. & Nazarov, Y. V. Spin-flip transitions between Zeeman sublevels in semiconductor quantum dots. *Phys. Rev. B* **64,** 125316 (2001).
28. Golovach, V. N., Khaetskii, A. & Loss, D. Phonon-induced decay of the electron spin in quantum dots. Preprint at ⟨http://xxx.lanl.gov/abs/cond-mat/0310655⟩ (2003).
29. Woods, L. M., Reinecke, T. L. & Lyanda-Geller, Y. Spin relaxation in quantum dots. *Phys. Rev. B* **66,** 161318 (2002).
30. Erlingsson, S. I. & Nazarov, Y. V. Hyperfine-mediated transitions between a Zeeman split doublet in GaAs quantum dots: The role of the internal field. *Phys. Rev. B* **66,** 155327 (2002).

Supplementary Information accompanies the paper on **www.nature.com/nature**.

Acknowledgements We thank D. P. DiVincenzo, H. A. Engel, T. Fujisawa, V. Golovach, Y. Hirayama, D. Loss, T. Saku, R. Schouten and S. Tarucha for technical support and discussions. This work was supported by the DARPA-QUIST programme, the ONR, the EU-RTN network on spintronics and the Dutch Organisation for Fundamental Research on Matter (FOM).

Competing interests statement The authors declare that they have no competing financial interests.

Correspondence and requests for materials should be addressed to L.M.K.V. (lieven@qt.tn.tudelft.nl).

Electrical detection of the spin resonance of a single electron in a silicon field-effect transistor

M. Xiao[1], I. Martin[2], E. Yablonovitch[3] & H. W. Jiang[1]

[1]*Department of Physics and Astronomy, University of California, Los Angeles, California 90095, USA*
[2]*Theoretical Division, Los Alamos National Laboratory, Los Alamos, New Mexico 87545, USA*
[3]*Department of Electrical Engineering, University of California, Los Angeles, California 90095-1594, USA*

The ability to manipulate and monitor a single-electron spin using electron spin resonance is a long-sought goal. Such control would be invaluable for nanoscopic spin electronics, quantum information processing using individual electron spin qubits and magnetic resonance imaging of single molecules. There have been several examples[1,2] of magnetic resonance detection of a single-electron spin in solids. Spin resonance of a nitrogen-vacancy defect centre in diamond has been detected optically[3], and spin precession of a localized electron spin on a surface was detected[4,5] using scanning tunnelling microscopy. Spins in semiconductors are particularly attractive for study because of their very long decoherence times[6]. Here we demonstrate electrical sensing of the magnetic resonance spin-flips of a single electron paramagnetic spin centre, formed by a defect in the gate oxide of a standard silicon transistor. The spin orientation is converted to electric charge, which we measure as a change in the source/drain channel current. Our set-up may facilitate the direct study of the physics of spin decoherence, and has the practical advantage of being composed of test transistors in a conventional, commercial, silicon integrated circuit. It is well known from the rich literature of magnetic resonance studies that there sometimes exist structural paramagnetic defects[7] near the Si/SiO_2 interface. For a small transistor, there might be only one isolated trap state that is within a tunnelling distance of the channel, and that has a charging energy close to the Fermi level.

When a defect is present, the source/drain channel current can experience random telegraph signal (RTS), jumping between two discrete current values. These arise from two possible trapped electric charge states of the defect. The two charge states can correspond to the two spin orientations of a trapped electron. Field effect transistor (FET) current senses electrostatic charge (by definition), and can thus sense single-electron spin resonance.

In view of the high degree of perfection of silicon devices, 80% of the transistors that we tested actually had no such trap states at all. In those cases we applied a high voltage spike to the gate in an attempt to induce a paramagnetic defect for study. Electron spin in low-transition-temperature semiconductors is now recognized[8] to have considerable potential for storing and manipulating quantum information. Some proposed qubit architectures trap electron spin in a controlled potential well[9] at the Si–Ge interface[10] and use transistor-like structures[11] for sensing.

Figure 1a sketches a simplified version of the transistor device in our experiment. The essential requirement for detecting a single spin flip is the conversion of spin-orientation to electric charge. In our approach, the Fermi level is adjusted so that it lies between the upper and lower Zeeman levels as illustrated in Fig. 1b. If the lower Zeeman level is occupied by one electron, as in Fig. 1b, it cannot accept any additional electrons from the Fermi level. If only the upper Zeeman level is occupied, as in Fig. 1c, then an additional electron can be transferred from the Fermi sea to the lower Zeeman level. The distinction between two trapped charges $2e^-$ (in Fig. 1c) versus one trapped charge $1e^-$ (in Fig. 1b) can be sensed, because an FET is basically an electrometer. Thus spin orientation is converted to electric charge, which is sensed by the source/drain current in an FET transistor.

Our n-channel Si transistors are operated near pinch-off, where the channel size is roughly 300 nm wide × 240 nm long. The signature of a single trap state is shown in the RTS source/drain current of Fig. 2a. Superimposed on the monotonically increasing background source/drain current is stochastic switching between two discrete values of channel current. This switching is the well-known RTS (for a comprehensive review, see ref. 12) that is a hallmark of the capture and emission of one electron by a single trap state. The well-defined RTS evolution in Fig. 2a demonstrates that over the 690 to 740 mV range, the trap is energetically well isolated from other traps.

A filled trap implies electrostatic repulsion that diminishes the channel current. At high gate voltages (near point A in Fig. 2a), the Fermi level E_F is well above the trap level E_T. Thus the trap is almost always filled, repelling electrons and allowing less current to flow in the source/drain channel. In contrast, at low gate voltages (near point C in Fig. 2a) when E_F is well below E_T, the trap is empty most of the time and the high current state is more probable. At the midpoint, when $E_F \approx E_T$ (near point B in Fig. 2a) the probability of the trap filling is about 50%. Thus the source/drain current senses the charge state of the trap.

The trap studied here is a very stable defect because the behaviour is reproducible over many thermal cycles from room temperature to liquid He^3 temperatures. From the signal-to-noise ratio, we find that the charge sensitivity of the our data acquisition system is $\sim 10^{-4}\, e\, Hz^{-1/2}$.

The Zeeman shift of the single trap[13] can readily be identified by studying the trap energy shift of the point at which the probability of the trap filling is 50% (where E_F lines up with the trap energy E_T), as a function of magnetic field. Figure 2b shows the Zeeman shift of this point as a function of an in-plane magnetic field. The trap energy shift was inferred from the gate voltage shift by using the procedure in ref. 13.

On the basis of the sign of the Zeeman shift, ref. 13 shows that the charging transition transfers from a single-charge state $1e^-$ to a double-charge state $2e^-$; that is, the charging is $1 \rightarrow 2$ rather than $0 \rightarrow 1$. In the energy diagram of Fig. 1b, the empty trap is modelled as an unpaired electron (for example, a dangling bond) that occupies the level E_T (the central red dashed line). In the presence of the magnetic field B, the single-electron state undergoes Zeeman splitting, indicated by the two solid lines at energies $E_T \pm (1/2)E_Z$. At low temperatures and high fields, only the lower spin state is occupied. If E_F is raised, an additional electron from the channel can tunnel into the upper spin state in Fig. 1b, forming a two-electron singlet state (for example, a lone pair). Thus the Fermi energy required for forming the two-electron state would increase when B is increased, as suggested by Fig. 2b. In contrast, an initially 'spinless' empty trap would fill the lower Zeeman level, producing the opposite field dependence—that is, the required Fermi energy would decrease with increasing B, contrary to observation. Therefore the initial empty trap begins in a $1e^-$ paramagnetic state ($S = 1/2$) (high current state) while the filled trap (lower current state) is a $2e^-$ singlet state.

Our electron spin resonance (ESR) detection scheme is based on the changing balance between the two source/drain current states of the transistor, when the Larmor precession frequency produces spin flips. In effect, this is transistor-current-detected ESR, as illustrated in Fig. 1c. When the paramagnetic spin flips, the lower Zeeman level becomes available for trapping an additional electron. The trapping event diminishes the average source/drain current. A rate equation analysis of this trap/channel configuration gave[14] the ESR-induced change in trap-filling probability.

To detect the ESR-microwave-induced change, we measured channel current at a fixed microwave frequency for 300 ms, during which there are about a few thousand RTS switching events, yielding good statistics for the average source/drain current. Figure 3a represents a fragment of such a trace over a 1 ms time interval. To complete the current versus magnetic field dependence, full 300-ms traces are taken at 150–250 different magnetic fields.

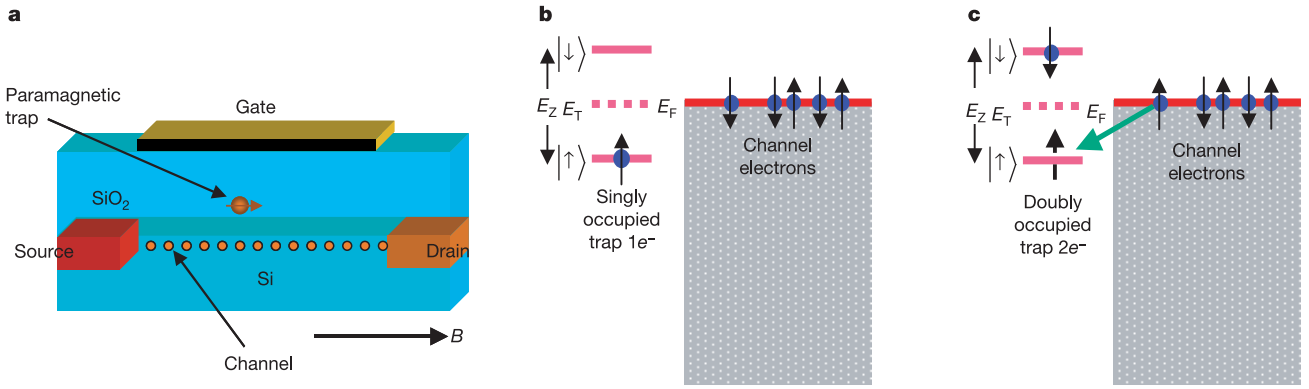

Figure 1 The mechanism for spin-to-charge conversion. **a**, A single paramagnetic trap, situated in a standard commercial n-channel Si FET that constitutes our sample. **b**, The Zeeman-split trap level relative to the FET channel Fermi level. The Fermi level would have to shift towards the upper Zeeman level to reach 50% occupation probability. (The singly occupied state should actually be down-shifted by the Coulomb correlation energy U, not shown.) **c**, If the spin flips under ESR, the lower Zeeman level can become filled, producing the doubly occupied trap.

Because the signals are sometimes noisy, a systematic statistical procedure was used to measure the trap charge state. A histogram of the source/drain current data versus time was plotted as shown in Fig. 3c. In the histogram, the empty and filled trap states are represented by the large and small peak, respectively. For the perfect case of two discrete states, we expect two narrow peaks in the histogram. The broadening of the peaks in Fig. 3c is caused by noise. The charge trapping probability ratio is proportional to the area ratio of the two peaks. For certain traps, whose charge produces only a small change in source/drain channel current, an additional step was taken to avoid noise errors. A sophisticated algorithm[15], for detection of abrupt step changes, was executed numerically. Figure 3a is the raw RTS, containing noise, whereas Fig. 3b shows the noiseless two-state switching, reconstructed by the algorithm.

We now present the ESR detection results for the single paramagnetic trap. Figure 4a shows the change in average source/drain current induced by a microwave frequency of 45.1 GHz. In Fig. 4a, an ESR peak in average current is centred around 16,025 G. Averaging blocks of four adjacent magnetic fields, the signal/noise ratio is >4:1, and the ESR feature is reproducible in different runs, and for different traps, in different samples.

We find that the ESR signal is most pronounced in the range of gate voltages corresponding to a paramagnetic (nearly empty) trap (that is, between points B and C in Fig. 2a). This is consistent with our assignment of filled and empty trap states.

The ESR signature is only found at temperatures below about 1 K. At those temperatures, the electron magnetic moment is substantially polarized, and in any case, microwave heating limits the temperature. From the RTS Boltzmann occupation probability as a function of voltage[13], we find that the effective temperature rises to about 1.5 K when a moderate microwave power of 0.1 mW is applied to the sample, even though the bath temperature still remains at about 0.4 K. The sensitivity of our time-averaged readout is thus limited by the microwave heating. From our signal-to-noise ratio, we estimate that our ESR signal could be read in a single shot, if the ESR were driven by a pulsed 180-GHz source. In the future, heating can be avoided by using g-tensor modulation[16,17] for single spin rotation.

Similar runs have been carried out at other frequencies and in various samples. The ESR magnetic resonance as a function of microwave frequency is plotted in Fig. 4b. For $hf = g\mu_B B$, a g-factor of 2.02 ± 0.015 is obtained. For a g-factor reference we used both a bulk Si crystal doped with 2×10^{18} cm^{-3} phosphorous; and the channel electrons in our n-channel Si transistor (Fig. 1a). Both agreed with the well-established values of $g \approx 1.998$. Because conduction electrons always[18] have $g < 2$, and paramagnetic centres in SiO_2 always[7] have $g > 2$, our results indicate a paramagnetic centre in the oxide, or at the SiO_2/Si interface. Our observed g-value is somewhat larger than that for some known paramagnetic centres near the Si/SiO_2 interface. A P_b paramagnetic centre is known to

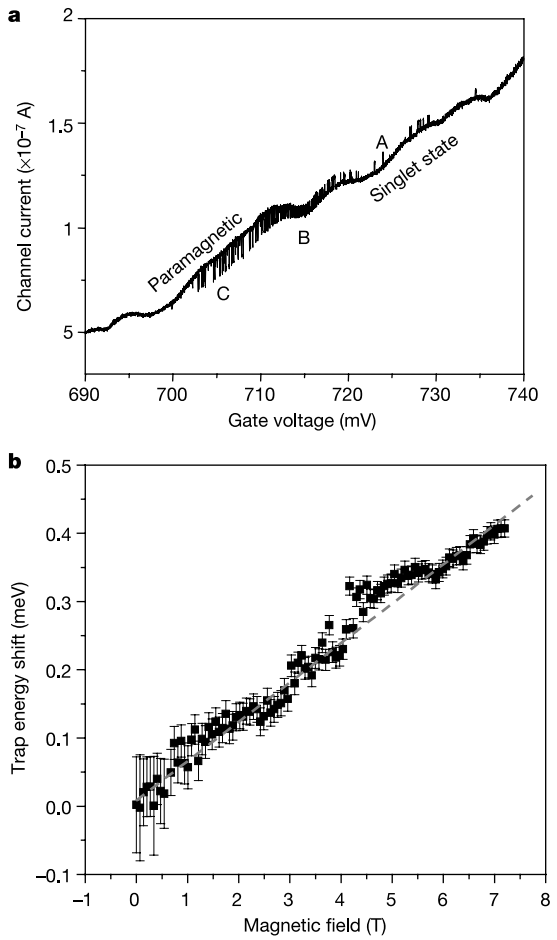

Figure 2 Random telegraph signal senses the defect energy level. **a**, The channel current I was recorded over a narrow gate voltage ramp from 690–740 mV, swept in a 30-ms time interval, with a 1-mV source/drain bias voltage at 1.3 K. The discrete upper and lower current states sense the two charge states, which can monitor the two electron spin states. **b**, The positive Zeeman shift of the trap energy versus magnetic field implies a $1e^-$ to $2e^-$ transition in the defect, rather than a $0e^-$ to $1e^-$ transition. The error bars indicate the standard deviation in the raw data.

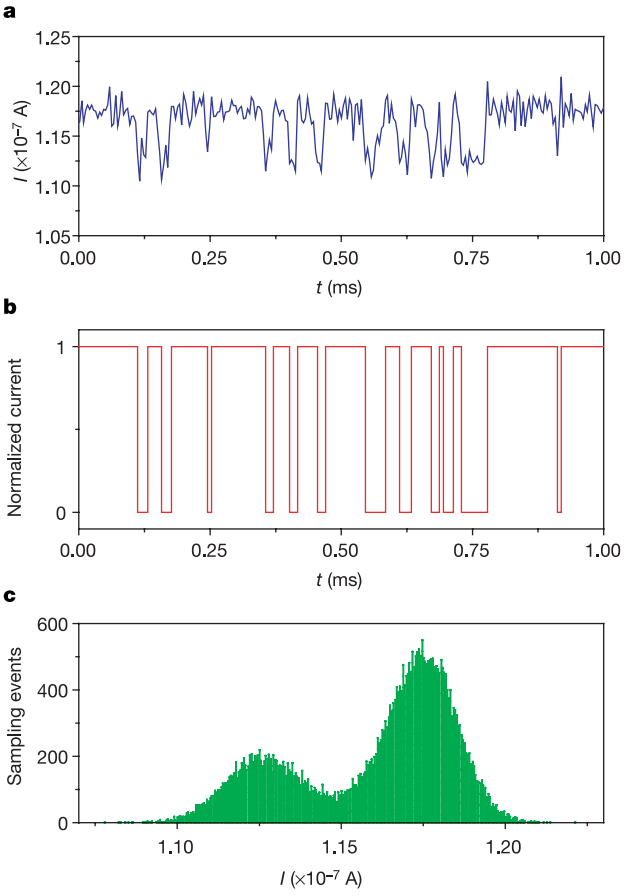

Figure 3 Detailed analysis of the random telegraph signal. **a**, The raw random telegraph data displayed for a time interval of 1 ms. **b**, An algorithm for detection of abrupt changes is applied to the raw data to reconstruct the two RTS levels. This procedure reduces the statistical errors due to noise. **c**, A histogram of the time-domain data. The large and small peaks represent the empty and filled trap states, respectively.

have a g-factor of 2.006 along the ⟨100⟩ direction, whereas the E′ centre is expected to have $g = 2.001$. One possibility is that we are looking at a centre that has a local structure different from that of these two typical examples. Another possibility is that the low-density conduction channel electrons might have slight ferromagnetic ordering, giving rise to a local field that slightly increases the apparent g-factor of the trap.

The full-width, half maximum linewidth of the observed resonance is about 5–10 G, which corresponds to the spin-spin relaxation time T_2 of about 0.1 μs. This time is much less than the typical 100-μs lifetime for isolated paramagnetic spins (the paramagnetic E′ centre in irradiated fused quartz has a T_2 of about 25 μs at room temperature; see for example, ref. 19) in SiO_2. There might be additional decoherence caused by the conduction electrons in the channel, or it might be caused by power broadening. Indeed, our microwave power produces a Rabi frequency $\gamma H_1 \approx 10$ kHz, comparable to the trap tunnelling time of about 20 kHz, where γ is the gyromagnetic ratio and H_1 is the microwave B field. For actual quantum information processing, the source/drain channel should only be un-pinched at the end of a quantum computation for readout, well within the T_1 lifetime.

At the strong Rabi frequency of $\gamma H_1 \approx 10$ kHz that is present at the end plate of our rectangular waveguide, nonlinear effects emerge. At lower microwave powers $\gamma H_1 \approx 1$ kHz, the single-occupancy trap probability is correctly observed to diminish under ESR, as expected from the reasoning in Fig. 1c. However at higher powers, $\gamma H_1 \approx 10$ kHz, the ESR-induced-current signal inverts, leading to an increase in occupancy trap probability, as plotted in Fig. 4a. We plotted the signal at high microwave power because it has a better signal-to-noise ratio.

We also see a nonlinear ESR response in the tunnelling dynamics. As shown in Fig. 5, the frequency of RTS jumps, which is proportional to the tunnelling rate, can change as much as 10% at the ESR condition. At low microwave power, $\gamma H_1 \approx 1$ kHz, the tunnelling rate increases at resonance, but at high Rabi frequency, $\gamma H_1 \approx 10$ kHz, the tunnelling rate inverts, as shown in Fig. 5. These inverted signals in both the source/drain current, and the tunnelling frequency, are only observed for high Rabi frequencies that are comparable to the tunnelling frequency. The nonlinear ESR response may be partly associated with non-resonant microwave-induced changes in the tunnelling rate, but we have not yet identified the dominant nonlinear mechanism.

Our evidence in support of the ESR signal arising from a single electron is summarized as follows: (1) The ESR signature is only observed in the random telegraph signal crossover region, predominantly between points B and C of Fig. 2a. (2) The random telegraph signal switching statistics, and thermal occupation probabilities, correspond to those of a single defect. (3) The g-factor value rules out channel electrons. The experiment demonstrates that an FET channel can effectively monitor the magnetic resonance of an adjacent single spin. □

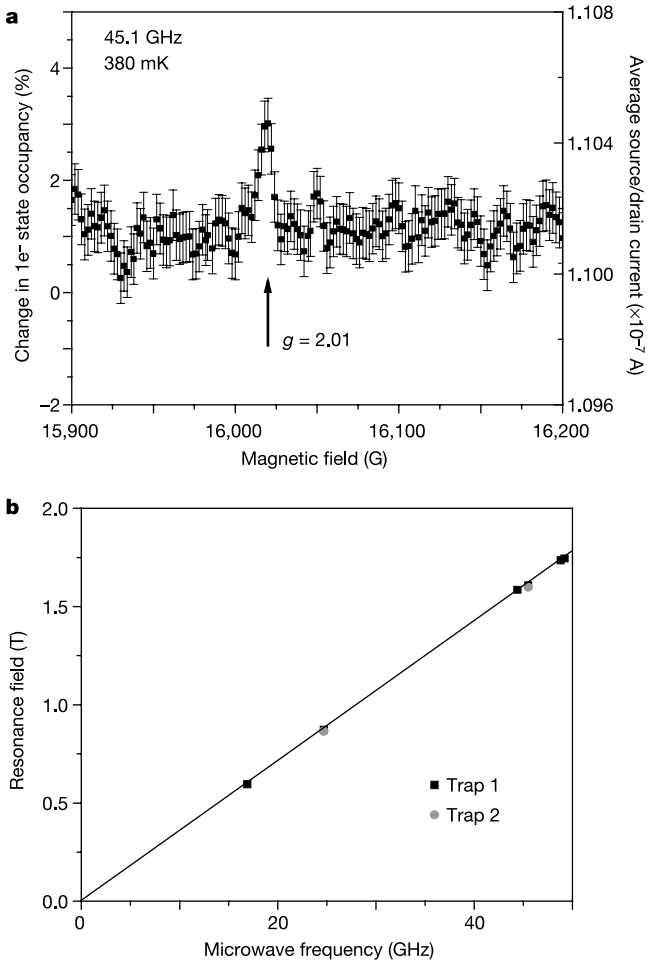

Figure 4 The single electron ESR signal. **a**, The single-occupancy trap probability, and the average source/drain current, versus magnetic field for a fixed microwave frequency. The peak represents electron spin resonance. The error bars (about 1%) indicate the standard deviation in a 300-ms data set averaged over four adjacent magnetic fields. **b**, The linear relationship of resonant magnetic field versus microwave frequency indicates a g-factor of 2.02 ± 0.015.

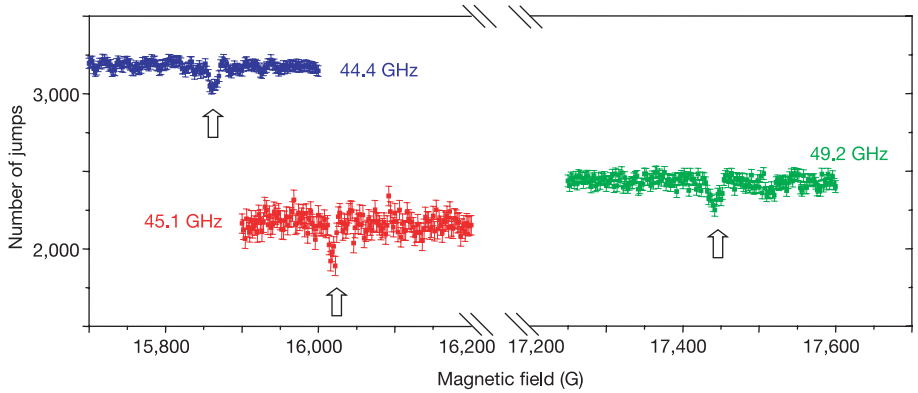

Figure 5 ESR induced change in tunnelling rates. The tunnelling rate between charge states is also substantially modified (~10% change) at ESR. The number of transitions, over a 300-ms time interval, between the paramagnetic and singlet states is plotted as a function of field for three different microwave frequencies. The resonance positions are marked by the vertical arrows. The error bars represent the standard deviation in the given data set.

Received 5 April; accepted 7 June 2004; doi:10.1038/nature02727.

1. Köhler, J. *et al.* Magnetic resonance of a single molecular spin. *Nature* **363,** 242–244 (1993).
2. Wrachtrup, J., von Borczyskowski, C., Bernard, J., Orrit, M. & Brown, R. Optical detection of magnetic resonance in a single molecule. *Nature* **363,** 244–245 (1993).
3. Jelezko, F., Gaebel, T., Popa, I., Gruber, A. & Wrachtrup, J. Observation of coherent oscillations in a single electron spin. *Phys. Rev. Lett.* **92,** 076401 (2004).
4. Manassen, Y., Hames, R. J., Demuth, J. E. & Castellano, A. J. Direct observation of the precession of individual paramagnetic spins on oxidized silicon surfaces. *Phys. Rev. Lett.* **62,** 2531–2534 (1989).
5. Durkan, C. & Welland, M. E. Electronic spin detection in molecules using scanning-tunneling-microscopy-assisted electron-spin resonance. *Appl. Phys. Lett.* **80,** 458–460 (2002).
6. Tyryshkin, A. M., Lyon, S. A., Astashkin, A. V. & Raitsimring, A. M Electron spin relaxation times of phosphorus donors in silicon. *Phys. Rev. B* **68,** 193207 (2003).
7. Poindexter, E. H. in *Semiconductor Interfaces, Microstructure, and Devices* (ed. Feng, Z. C.) Ch. 10, 229–256 (Inst. Phys. Publ., Bristol, Philadelphia, 1993).
8. Loss, D. & DiVincenzo, D. P. Quantum computation with quantum dots. *Phys. Rev. A.* **57,** 120–126 (1998).
9. Friesen, M. *et al.* Practical design and simulation of silicon-based quantum-dot qubits. *Phys. Rev. B* **67,** 121301 (2003).
10. Vrijen, R. *et al.* Electron-spin-resonance transistors for quantum computing in silicon-germanium heterostructures. *Phys Rev. A* **62,** 012306 (2000).
11. Kane, B. E. A silicon based nuclear spin quantum computer. *Nature* **393,** 133–137 (1998).
12. Kirton, M. J. & Uren, M. J. Noise in solid-state microstructures: a new perspective on individual defects, interface states and low-frequency (1/f) noise. *Adv. Phys.* **38,** 367–468 (1989).
13. Xiao, M., Martin, I. & Jiang, H. W. Probing the spin state of a single electron trap by random telegraph signal. *Phys. Rev. Lett.* **91,** 078301 (2003).
14. Martin, I., Mozyrsky, D. & Jiang, H. W. A scheme for electrical detection of single electron spin resonance. *Phys. Rev. Lett.* **90,** 018301 (2003).
15. Liu, W., Ji, Z., Pfeiffer, L., West, K. W. & Rimberg, A. J. Real-time detection of electron tunnelling in a quantum dot. *Nature* **423,** 422–425 (2003).
16. Kato, Y. *et al.* Gigahertz electron spin manipulation using voltage-controlled g-tensor modulation. *Science* **299,** 1201–1204 (2003).
17. Yablonovitch, E. *et al.* Optoelectronic quantum telecommunications based on spins in semiconductors. *Proc. IEEE* **91,** 761–780 (2003).
18. Wallace, W. J. & Silsbee, R. Spin resonance of inversion-layer electrons in silicon. *Phys. Rev. B* **44,** 12964–12968 (1991).
19. Eton, S. S. & Eaton, G. R. Irradiated fused-quartz standard sample for time-domain EPR. *J. Magn. Res. Ser. A* **102,** 354–356 (1993).

Acknowledgements We would like to thank P. M. Lenahan for information regarding the relaxation of spin centres in SiO_2, and K. Wang for helping to secure the samples. The work was supported by the Defense Advanced Research Projects Agency and the Defense MicroElectronics Activity.

Competing interests statement The authors declare that they have no competing financial interests.

Correspondence and requests for materials should be addressed to H.W.J. (jiangh@physics.ucla.edu).

Surface transfer doping of diamond

P. Strobel, M. Riedel, J. Ristein & L. Ley

Institute for Technical Physics, University of Erlangen, 91054 Erlangen, Germany

The electronic properties of many materials can be controlled by introducing appropriate impurities into the bulk crystal lattice in a process known as doping. In this way, diamond (a well-known insulator) can be transformed into a semiconductor[1], and recent progress in thin-film diamond synthesis has sparked interest in the potential applications of semiconducting diamond[2,3]. However, the high dopant activation energies (in excess of 0.36 eV) and the limitation of donor incorporation to (111) growth facets only have hampered the development of diamond-based devices. Here we report a doping mechanism for diamond, using a method that does not require the introduction of foreign atoms into the diamond lattice. Instead, C_{60} molecules are evaporated onto the hydrogen-terminated diamond surface, where they induce a sub-surface hole accumulation and a significant rise in two-dimensional conductivity. Our observations bear a resemblance to the so-called surface conductivity of diamond[4–8] seen when hydrogenated diamond surfaces are exposed to air, and support an electrochemical model in which the reduction of hydrated protons in an aqueous surface layer gives rise to a hole accumulation layer[6,7]. We expect that transfer doping by C_{60} will open a broad vista of possible semiconductor applications for diamond.

The C_{60} was evaporated onto differently prepared diamond surfaces and onto a silica glass substrate. After each evaporation step the conductance of the respective sample was measured as described below and without breaking the vacuum. The closed symbols in Fig. 1 refer to the conductance of two different homoepitaxial diamond samples with hydrogenated surfaces as a function of C_{60} coverage in a double-logarithmic plot. The starting point is in both cases the annealed state (see Methods) with a conductance well below 10^{-12} S (leftmost data point). With increasing C_{60} coverage the conductance rises rapidly by more than six orders of magnitude and saturates at 10^{-6} S for sample D20 and 10^{-5} S for sample D34 at a C_{60} coverage between 4 and 8 monolayers (ML). Two control experiments (open symbols) were performed with silica glass and with diamond sample D20, this time with an oxidized instead of a hydrogenated surface as the substrate for C_{60} evaporation. The negative results presented in Fig. 1 confirm that the conductivity necessarily requires the combination of C_{60} and hydrogenated diamond; the C_{60} layer alone on an insulating substrate (glass) or in combination with an oxidized diamond surface is not sufficient.

We propose that the cause of the observed conductivity is a transfer doping mechanism whereby electrons are transferred from diamond to the C_{60} layer such that an equal amount of electrons and holes reside on the C_{60} and diamond side of the interface, respectively. For this to work, the energy level scheme as sketched in Fig. 2a has to be considered. The left-hand part depicts the valence and conduction band edges (VBM and CBM) of diamond, together with the Fermi level E_F. On the right-hand side a limited number of occupied and unoccupied molecular orbitals of C_{60} are schematically sketched with the highest occupied (HOMO) and the lowest unoccupied (LUMO) bracketing the fundamental gap of C_{60}. The common reference level is the vacuum level E_{VAC}. For hydrogen-terminated diamond the electron affinity is negative, that is, the CBM lies 1.3 eV above E_{VAC} (refs 9, 10). The electron affinity $E_{VAC} - E_{LUMO}$ of C_{60} is measured to be about 2.7 eV for the C_{60} molecule[11], and this places the Fermi level of C_{60}, which lies between the HOMO and the LUMO, well below the E_F of diamond. Hence,

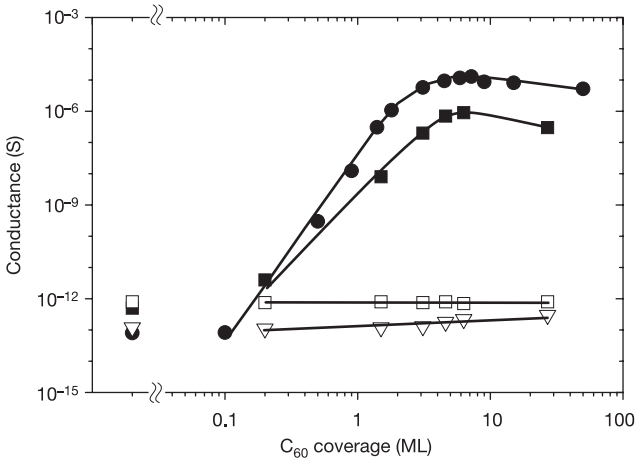

Figure 1 Conductance of different substrates upon evaporation of C_{60} in ultrahigh vacuum. Filled circles and squares, hydrogen-terminated diamond, samples D20 and D34, respectively. Open squares, oxygen-terminated diamond; open triangles, silica glass. The leftmost data points correspond to the clean surfaces after mild annealing at about 250 °C. Note the logarithmic scales of the plot. The C_{60} coverage is given in ML; 1 ML corresponds to an areal density of 1.15×10^{14} C_{60} molecules per cm^2. The lines through the data points are guides to the eye.